

Towards Cell-Free Massive MIMO: A Measurement-Based Analysis

DAVID LÖSCHENBRAND, (Member, IEEE), MARKUS HOFER, (Member, IEEE), LAURA BERNADÓ, (Member, IEEE), STEFAN ZELENBABA, (Member, IEEE), and THOMAS ZEMEN, (Senior Member, IEEE)

AIT Austrian Institute of Technology GmbH, Giefinggasse 4, 1210 Vienna, Austria (e-mail: firstname.lastname@ait.ac.at)

Corresponding author: David Löschénbrand (e-mail: david.loeschenbrand@ait.ac.at).

This paper is a result of the project DEDICATE (dedicate.ait.ac.at). The DEDICATE project is funded within the Principal Scientist grant "Dependable Wireless 6G Communication Systems" at the AIT Austrian Institute of Technology. This work has been submitted to the IEEE for possible publication. Copyright may be transferred without notice, after which this version may no longer be accessible

ABSTRACT Cell-free widely distributed massive multiple-input multiple-output (MIMO) systems utilize radio units spread out over a large geographical area. The radio signal of a user equipment (UE) is coherently detected by a subset of radio units (RUs) in the vicinity of the UE and processed jointly at the nearest baseband processing unit (BPU). This architecture promises two orders of magnitude less transmit power, spatial focusing at the UE position for high reliability, and consistent throughput over the coverage area. All these properties have been investigated so far from a theoretical point of view. To the best of our knowledge, this work presents the first empirical radio wave propagation measurements in the form of time-variant channel transfer functions for a linear, widely distributed antenna array with 32 single antenna RUs spread out over a range of 46.5 m. The large aperture allows for valuable insights into the propagation characteristics of cell-free systems. Three different co-located and widely distributed RU configurations and their properties in an urban environment are analyzed in terms of time-variant delay-spread, Doppler spread, path loss and the correlation of the local scattering function over space. For the development of 6G cell-free massive MIMO transceiver algorithms, we analyze properties such as channel hardening, channel aging as well as the signal to interference and noise ratio (SINR). Our empirical evidence supports the promising claims for widely distributed cell-free systems.

INDEX TERMS Cell-free massive MIMO, non-stationary propagation conditions, widely distributed antenna elements,

I. INTRODUCTION

CELL-FREE massive multiple-input multiple-output (MIMO) systems are a revolutionary new architecture for future mobile communications systems [1]. Radio units (RUs) are distributed in space over a large geographical area and processed coherently at a central baseband processing unit (BPU). This architecture enables similar properties as known from massive MIMO systems such as high spectral efficiency using linear processing and exploiting channel reciprocity between uplink and downlink. However, key additional properties are obtained by the distribution of RUs in space, such as (i) a strong transmit energy reduction due to reduced distance to the user equipment (UE), (ii) a consistent throughput over the coverage area avoiding the strong throughput drop at cell edges, and (iii) mitigation of large-scale fading [2].

So far, cell-free massive MIMO systems have been explored from a theoretical point of view (see [1] and the references therein). Empirical evidence on propagation conditions in cell-free systems is missing although of fundamental importance. Cell-free systems can be seen as a distributed antenna array with a large aperture, causing common far-field assumptions (e.g. plane wave propagation) to not hold and propagation conditions to differ substantially from RU to RU. In other words, the propagation conditions for mobile users are non-stationary in space and time.

In this work we use a software-defined radio (SDR) based measurement system for characterizing the propagation conditions in cell-free massive MIMO systems with mobile users. A distributed massive MIMO testbed was established at AIT Austrian Institute of Technology [3]. The architecture of [3] allows fully parallel radio channel measurements for

vehicular users as well as data transmission including channel prediction [4]. For widely distributed and cell-free radio channel measurements, the architecture of [3] is extended, enabling a distribution of antenna elements over up to 90 m. This is achieved by separating the down-conversion from radio frequency (RF) to baseband into a distributed unit (DU) and performing baseband processing in a BPU. Phase coherent operation is achieved by a dedicated synchronization network using a 10 MHz clock and a one pulse per second signal with dedicated distribution circuits.

A. RELATED WORK AND LITERATURE OVERVIEW

The research work on cell-free massive MIMO has increased tremendously over the last five years, see e.g. [1], [2], [5], [6] and the references therein, as it is considered an enabling technology for beyond 5G systems. While anticipated key characteristics are already known through extensive analysis and simulation, empirical validation is largely missing.

Wireless propagation channel measurements with a virtual wide-aperture array at 2.6 GHz with an aperture size of 7.3 m were first reported in [7]. The proposed measurement approach involves one antenna that is moved to form a virtual array and is only suitable for static scenarios without mobility.

In [8] the authors describe a comparative study of MIMO antenna geometries, with aperture sizes ranging from 0.3 m to 6 m. Eight fully parallel receive units and fast switching was used to characterize the system with 64 base station (BS) antenna elements.

A first cell-free channel measurement was reported in [9] using a drone with a single transmit antenna, flying from one RU position to the next. This method does not provide coherent impulse responses from the RU positions but allows a quantitative assessment of properties such as the uplink energy efficiency [10]. Furthermore, UE mobility and scatterer mobility cannot be captured by the distributed virtual array measurement principle of [9].

B. CONTRIBUTIONS OF THIS WORK

- World-first fully parallel and coherent widely distributed array channel sounding measurements in high mobility scenario with 32 BS antennas and two users.
- Comparative analysis of wireless propagation conditions for BS aperture sizes from 2 m to 46.5 m in terms of delay spread, Doppler spread, received power, and collinearity of the local scattering function (LSF).
- Evaluation of channel hardening and effects of channel aging on the signal to interference and noise ratio (SINR) in a cell-free massive MIMO system based on the obtained measurement data.

C. ORGANIZATION OF THIS WORK

The paper is organized as follows. Section II describes the measurement scenario and the measurement framework utilized for this purpose. In Section III the signal model for the obtained data is introduced and the necessary parameters for

evaluation are defined. Section IV presents the corresponding results. Section V introduces the signal model for a cell-free massive MIMO system and describes the effects of channel aging and channel hardening based on the obtained measurement results.

II. SCENARIO DESCRIPTION AND MEASUREMENT FRAMEWORK

We report a widely distributed massive MIMO channel sounding campaign that was conducted in March 2022 at the premises of AIT Austrian Institute of Technology GmbH in Vienna, Austria. In this campaign, three different array geometries with apertures ranging from 2 m to 46.5 m were installed and tested. We thereby analyze the merits and drawbacks of widely distributed and cell-free systems in comparison to conventional massive MIMO systems currently being deployed and operational worldwide.

Massive MIMO systems are especially suitable for dealing with urban environments with multipath propagation, since the large number of RUs allows for spatial focusing and spatial separation of users. However, mobility is still problematic as it generally leads to outdated channel state information (CSI) for beam-forming when not properly accounted for [4].

Cell-free systems are envisioned to be deployed in urban environments as they potentially mitigate the burden of large-scale fading, i.e. blocking by buildings, vegetation, cars etc. The cell-free massive MIMO channel sounding campaign is designed to capture these urban channel characteristics, including mobility, multipath propagation, blocking and transition from line of sight (LOS) to non line of sight (NLOS).

Two vertically polarized monopole transmit antennas are mounted on the rooftop of a van right above the driving seat and the passenger seat, respectively. They are acting as UEs transmitting a signal and are referenced in the following as UE_k with $k \in \{1, 2\}$. Users UE_k are following a fixed trajectory near the Austrian Institute of Technology GmbH (AIT) premises for all measurements, with velocities ranging from 15 km/h to 60 km/h on the straight part of the street. The trajectory is divided into eight regions R_s , $s \in \{1, \dots, 8\}$, with a length of approximately 40 m each, for easy referencing and location-specific data evaluation. Figure 1 shows a top view of the scenario under consideration, with the UE trajectory and the regions R_1 to R_8 indicated in blue. The starting position of the UEs is marked with a white van icon.

On the BS side, 32 RUs consisting of single patch antennas are positioned on the roof top of an office building at a height of 15 m as a horizontal linear array, with vertical polarization and their individual main lobe facing north. The RUs are receiving the signal transmitted by the UEs. The green area in Fig. 1 shows the position of the BS array. Since there is an office building of similar height to the north of the linear BS antenna array (in the directions the individual patch antenna array elements are pointing to), regions R_3 to R_5 of the UE trajectory are exhibiting NLOS conditions. Regions R_1 and R_2 are characterized as LOS with the main direction of UE movement perpendicular to the BS antenna array, while

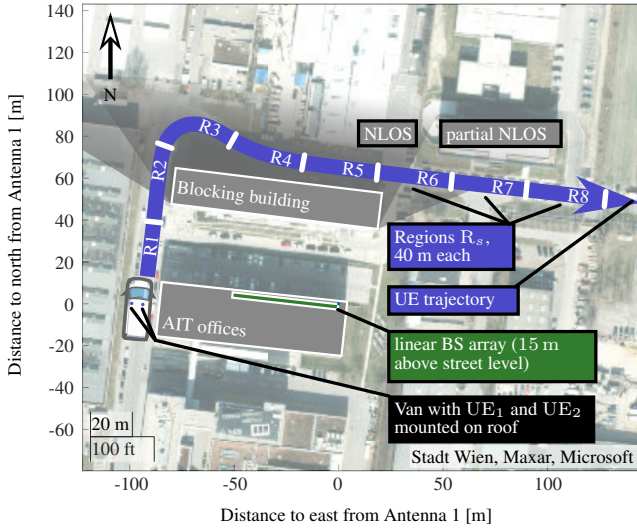


FIGURE 1: Top view of the measurement scenario. The UE trajectory is divided into regions R_1 to R_8 and indicated in blue. The BS antenna array is located on the roof of an office building and indicated in green. The individual RUs are facing a large office building to the north, dividing the UE trajectory into LOS and NLOS regions.

regions R_6 , R_7 , and R_8 show LOS characteristics with the main direction of UE movement parallel to the BS antenna array. The region where the blocking building causes NLOS conditions and the transition to LOS is indicated as a gray shade in Fig. 1.

Three different linear horizontal BS array configurations are implemented, with significant variation in the array aperture and antenna element spacing. Figure 2 shows in green the position where all three array configurations are located. As a reference point, the easternmost antenna 1 stayed on the same position throughout all measurements. The white elements in the green bars at the top of Fig. 2 indicate the individual position and spacing of antenna elements for the three array configurations and will serve as reference and visualization aid throughout the remainder of this paper. The exact positioning and spacing of the patch antenna elements is detailed in the next section.

A. FLEXIBLE WIDE APERTURE ARRAY MEASUREMENT FRAMEWORK

A measurement framework based on our previous work in [3] is used to capture the sounding sequences emitted from users UE_k . In addition to each of the two DUs having a distance of up to 30 m to the central BPU and synchronization unit (as outlined in [3]), coaxial cables with a length of 15 m are used to connect each DU with 16 RUs (patch antenna array elements), see Fig. 3 at the bottom. With this method, array apertures of up to 90 m with 32 array elements are possible, all while maintaining fully parallel and fast channel sounding capabilities. To compensate for the losses of the long coaxial cables, power amplifiers with a 1 dB compression point of 39 dBm are used at the UE side.

With the BS setup as described above, different antenna array geometries can be realized with minimal effort. We

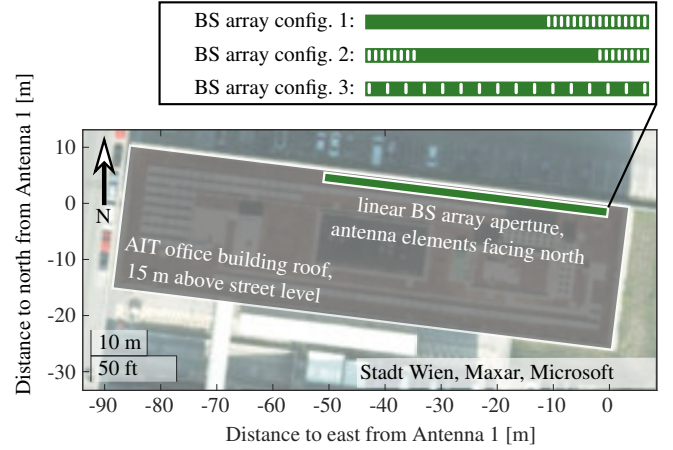


FIGURE 2: Top view of the roof where three different BS array configurations are realized. The white elements in the green bars at the top indicate the individual position and spacing of antenna elements for the three array configurations.

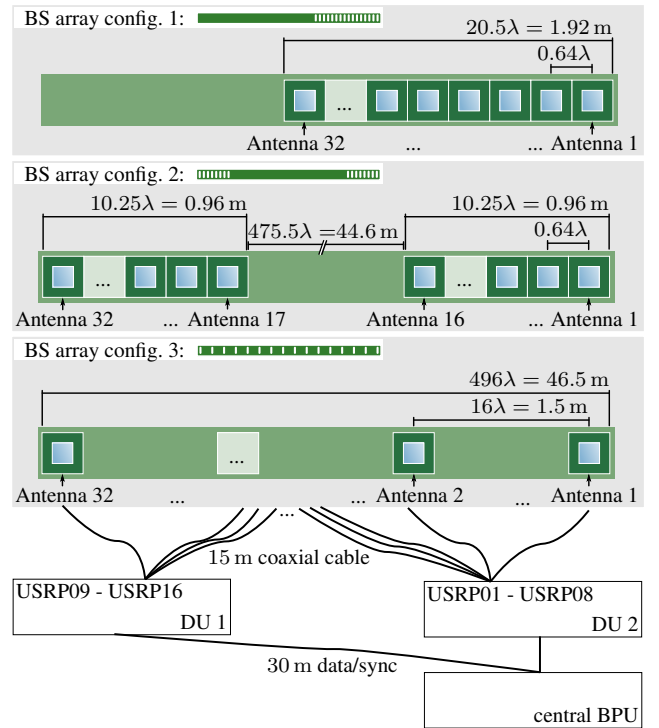


FIGURE 3: Channel measurement framework consisting of a central BPU for data aggregation and storage (bottom), two DUs for up- and down conversion, and 32 RUs assembled in one of three BS array configurations (top).

chose to implement three different horizontal linear arrays with varying aperture size and element spacing. Detailed array dimensions are provided in Fig. 3.

BS array configuration 1 (BS conf. 1) resembles a conventional linear massive MIMO array with 32 antenna elements aligned horizontally and spaced 0.64λ with λ being the wavelength at the sounding frequency of $f = 3.2$ GHz. With this array configuration, grating lobes are mostly avoided and the transmitting UEs operate in the far-field [11, Sec. 4] of the BS array, i.e. the distance d_k between UE_k and BS array

satisfies

$$d_k \geq \frac{2D^2}{\lambda} \quad (1)$$

with D being the size of the linear BS array. Large-scale fading and other channel statistics are expected to be very similar over the BS array aperture.

BS array configuration 2 (BS conf. 2) resembles a distributed massive MIMO array with two antenna arrays of 16 elements. The two arrays are distributed with a distance of 44.6 m between them. Each of the distributed arrays is again assembled with horizontally aligned and 0.64λ -spaced antenna elements. With this distributed array configuration and a total aperture size of 46.5 m, the UEs never operate in the far-field of the BS array according to (1). This implies that wavefronts impinging at the BS array are spherical in general and not of equal amplitude. Large-scale fading and other channel statistics are expected to be very similar for each distributed 16-element array on its own, but may differ greatly from one distributed array to the other.

BS array configuration 3 (BS conf. 3) resembles a cell-free massive MIMO setup with 32 antenna elements horizontally aligned, but spaced with a distance of 16λ from one array element to the next. Since the large aperture of 46.5 m is uniformly filled with receiving elements, each one of them is expected to exhibit variations in large-scale fading and other channel statistics due to their large spatial separation.

The parameters of the channel sounding framework utilized for the presented measurement campaign are listed in Table 1. For each BS array configuration, 10 runs on the same UE trajectory with similar velocities are performed. One measurement run lasts 30 s, in which a distance of around 300 m (divided in eight regions) is covered.

TABLE 1: Measurement parameters and their respective values.

Parameter	Value
carrier frequency f	3.2 GHz
number of tones Q	481
tone spacing Δf	240 kHz
bandwidth B	115.44 MHz
repetition rate T_R	1 ms
max. resolvable Doppler frequency	500 Hz
max. resolvable velocity	150 km/h
TX power	38 dBm
measurement time per run	30 s
runs per BS config.	10
UEs distance traveled	300 m

III. CHANNEL SOUNDING SIGNAL MODEL

With the channel sounding framework described above, we obtain bandlimited estimates of the wireless channel transfer function by transmitting a known sounding sequence from $K = 2$ users UE_k , receiving it at the $A = 32$ RUs simultaneously and storing the sampled time signal on a

hard-drive. In post-processing, this stored time signals are Fourier-transformed and calibrated to correct for the effects of the RF chain. The obtained time-dependent realizations of the channel matrix are then used to derive and analyze the channel characteristics. The procedure is detailed in the following (see also [3], [12]).

We use a complex baseband multitone signal

$$x[n] = x(nT/Q) = \sum_{q=-(Q-1)/2}^{(Q-1)/2} X[q] e^{i2\pi qn/Q} \quad (2)$$

to capture the channel characteristic over time. The time signal $x[n]$ is formed by a superposition of Q tones with complex weights $X[q]$ and frequency spacing Δf . The amplitudes of the complex weights are chosen to be equal, i.e. $|X[q]| = 1$. Their phases are optimized to achieve a low crest factor [13]

$$C = \frac{\max_{t \in [0, T]} |x(t)|}{\sqrt{\frac{1}{N} \int_0^T |x(t)|^2 dt}} \quad (3)$$

of the continuous signal $x(t)$ over the period $T = 1/\Delta f$ with the algorithm proposed in [14].

The multitone signal $x[n]$ utilized in this work features a frequency spacing of $\Delta f = 240$ kHz and $Q = 481$ tones, thus yielding a bandwidth of $B = 115.44$ MHz, with a crest factor $C = 1.24$. Similar to an orthogonal frequency-division multiplexing (OFDM) system, we concatenate the multitone signal with a copy of itself which acts as cyclic prefix (CP). Additionally, a third copy is added to increase the signal to noise ratio (SNR). Thus, the final sounding signal consists of three concatenated copies of the multitone signal $x[n]$ and therefore lasts $3T = 12.5$ μ s. Each user UE_k transmits the same sounding sequence with a $(k-1)3T$ time shift to not interfere with the current measurement.

The sounding signal is sent and received with a repetition rate of $T_R = 1$ ms which results in a maximum resolvable Doppler frequency of 500 Hz and a maximum resolvable UE velocity of 150 km/h at a sounding frequency of $f = 3.2$ GHz.

Each individual antenna $a \in \{1, 2, \dots, A\}$ of the BS receives the sounding signal (convolved with the propagation channel $\hat{H}_{a,k}[m, q]$) $\tilde{y}_{a,k}[m, n]$, transmitted by UE_k . Since the sounding procedure works similar to a CP OFDM scheme, the received multitone signal weights are obtained by omitting the CP and guard periods in $\tilde{y}_{a,k}[m, n]$ to obtain $y_{a,k}[m, n]$ and a subsequent discrete Fourier transformation, i.e.

$$Y_{a,k}[m, \tilde{q}] = \frac{1}{\sqrt{2Q}} \sum_{n=0}^{2Q-1} y_{a,k}[m, n] \exp^{-j\frac{2\pi n \tilde{q}}{2Q}}, \quad (4)$$

where m denotes discrete time and q discrete frequency.

The signal part of the sounding sequence contains two repetitions of the multitone signal (2). Therefore, every second bin $Y_{a,k}[m, q] = Y_{a,k}[m, 2\tilde{q}]$ constitutes the uncalibrated transfer function of the propagation channel and the radio front-ends. The transmitted symbols $X[q]$ are known at the

receiver and the calibrated transfer function estimate of the channel is thus obtained by

$$\hat{H}_{a,k}[m, q] = \frac{Y_{a,k}[m, q]}{X[q] \hat{H}_{a,k}^{\text{RF}}[q]}. \quad (5)$$

The transfer function $\hat{H}_{a,k}^{\text{RF}}[q]$ of the RF chains is obtained during a calibration phase prior to the measurement [3].

A. STATISTICAL CHARACTERIZATION OF THE WIRELESS PROPAGATION CHANNEL

To draw conclusions about wide-sense stationarity or the lack thereof for the BS array configurations under investigation, we revert to analyzing the moments of the wireless channels' power delay profile (PDP) and Doppler spectral density (DSD). To that end, the LSF is introduced as it provides a means of calculating the considered parameters in highly dynamic scenarios [15], [16].

A certain number of consecutive measurements M is necessary to calculate the LSF in (6). Therefore, a discrete time l is introduced to index the calculated LSFs and its moments and marginals. The time index l is often referred to in literature as the stationarity region index, while M is then the stationarity region length [15], [17] and chosen to be even in this work.

Given the time-variant frequency transfer function estimate $\hat{H}_{a,k}[m, q]$ from UE_k to BS antenna a , the estimate of the LSF at stationarity region index l is given as

$$\hat{C}_{a,k}[l; n, p] = \frac{1}{IJ} \sum_{w=0}^{IJ-1} \left| \mathcal{H}_{a,k}^{(G_w)}[l; n, p] \right|^2 \quad (6)$$

with the Doppler shift index $p \in \{-M/2, \dots, M/2 - 1\}$ and the delay index $n \in \{0, \dots, Q - 1\}$. The delay and Doppler shift resolution are defined by $\tau_s = \frac{1}{Q\Delta f}$ and $\nu_s = \frac{1}{MT_R}$, where T_R is the repetition rate of measurement. The operation $m = lM + m'$ maps the measurement time index m to the stationarity region index l . The tapered frequency response is

$$\begin{aligned} \mathcal{H}_{a,k}^{(G_w)}[l; n, p] &= \sum_{m=-M/2}^{M/2-1} \sum_{q=-(Q-1)/2}^{(Q-1)/2} \hat{H}_{a,k}[m' + Ml, q] \\ &\cdot G_w[m', q] e^{-j2\pi(pm' - nq)}, \end{aligned} \quad (7)$$

where the tapers $G_w[m, q]$ are two-dimensional discrete prolate spheroidal (DPS) sequences as shown in detail in [17], [18]. The number of tapers in the time and frequency domain is set to $I = 2$ and $J = 1$, respectively [17], [19].

We calculate the PDP and DSD as projections of the LSF onto the Doppler domain and the delay domain, respectively:

$$\hat{\mathcal{P}}_{a,k}^{(\tau)}[l; n] = \frac{1}{M} \sum_{p=-M/2}^{M/2-1} \hat{C}_{a,k}[l; n, p], \quad (8)$$

$$\hat{\mathcal{P}}_{a,k}^{(\nu)}[l; p] = \frac{1}{Q} \sum_{n=0}^{Q-1} \hat{C}_{a,k}[l; n, p]. \quad (9)$$

B. MOMENTS OF THE PDP AND DSD

The time-variant first moment of the PDP of the estimated channel transfer function $\hat{H}_{a,k}[m, q]$, i.e. its time-integrated power, is calculated as

$$\hat{\mathcal{P}}_{a,k}^{(\tau)}[l] = \sum_{n=0}^{Q-1} \hat{\mathcal{P}}_{a,k}^{(\tau)}[l; n]. \quad (10)$$

The second moment is referred to as the mean delay and calculated as

$$\bar{\tau}_{a,k}[l] = \frac{\sum_{n=0}^{Q-1} (n\tau_s) \hat{\mathcal{P}}_{a,k}^{(\tau)}[l; n]}{\hat{\mathcal{P}}_{a,k}^{(\tau)}[l]}. \quad (11)$$

We calculate the root mean square (RMS) delay spread by

$$\sigma_{a,k}^{(\tau)}[l] = \sqrt{\frac{\sum_{n=0}^{Q-1} (n\tau_s)^2 \hat{\mathcal{P}}_{a,k}^{(\tau)}[l; n]}{\hat{\mathcal{P}}_{a,k}^{(\tau)}[l]} - \bar{\tau}[l]^2}. \quad (12)$$

Similarly, with the integrated power

$$\hat{\mathcal{P}}_{a,k}^{(\nu)}[l] = \sum_{p=-M/2}^{M/2-1} \hat{\mathcal{P}}_{a,k}^{(\nu)}[l; p] \quad (13)$$

and the mean Doppler

$$\bar{\nu}_{a,k}[l] = \frac{\sum_{p=-M/2}^{M/2-1} (p\nu_s) \hat{\mathcal{P}}_{a,k}^{(\nu)}[l; p]}{\hat{\mathcal{P}}_{a,k}^{(\nu)}[l]} \quad (14)$$

we obtain the RMS Doppler spread by

$$\sigma_{a,k}^{(\nu)}[l] = \sqrt{\frac{\sum_{p=-M/2}^{M/2-1} (p\nu_s)^2 \hat{\mathcal{P}}_{a,k}^{(\nu)}[l; p]}{\hat{\mathcal{P}}_{a,k}^{(\nu)}[l]} - \bar{\nu}_{a,k}[l]^2}. \quad (15)$$

We define the time-dependent average received power at time instant l as the sum over the LSF in both time and frequency

$$\hat{\mathcal{P}}_{a,k}[l] = \frac{1}{MQ} \sum_{p=-M/2}^{M/2-1} \sum_{n=0}^{Q-1} \hat{C}_{a,k}[l; n, p] \quad (16)$$

$$= \frac{1}{Q} \hat{\mathcal{P}}_{a,k}^{(\tau)}[l] = \frac{1}{M} \hat{\mathcal{P}}_{a,k}^{(\nu)}[l]. \quad (17)$$

Let $L(s)$ denote the set of time indices l for which the user UE_k moves in a given region R_s , $s \in \{1, \dots, 8\}$ (see also Fig. 1). If user UE_k is in region R_s at time instant l , then $l \in L(s)$. The size of the set $L(s)$, representing the time a user spent in a given region, is denoted by $|L(s)|$. The average received power from user UE_k in region R_s is then defined as

$$\hat{\mathcal{P}}_{a,k}[s] = \frac{1}{|L(s)|} \sum_{l \in L(s)} \hat{\mathcal{P}}_{a,k}[l]. \quad (18)$$

For a more convenient exposition later on, we also define the normalized received power from user UE_k in region R_s by dividing with the maximum value of $\frac{1}{A} \sum_{a=1}^A \hat{\mathcal{P}}_{a,k}[s]$ over

all regions R_s , $s \in \{1, \dots, 8\}$,

$$\bar{\mathcal{P}}_{a,k}[s] = \frac{\hat{\mathcal{P}}_{a,k}[s]}{\max_s \frac{1}{A} \sum_{a=1}^A \hat{\mathcal{P}}_{a,k}[s]}. \quad (19)$$

C. COLLINEARITY OF THE LSF

We define the collinearity [16], [17] of the LSF at time index l

$$\gamma_{a,a',k}[l] = \frac{\sum_{p=-M/2}^{M/2-1} \sum_{n=0}^{Q-1} \hat{\mathcal{C}}_{a,k}[l; n, p] \odot \hat{\mathcal{C}}_{a',k}[l; n, p]}{\left\| \hat{\mathcal{C}}_{a,k}[l; n, p] \right\|_F \left\| \hat{\mathcal{C}}_{a',k}[l; n, p] \right\|_F}, \quad (20)$$

with

$$\left\| \hat{\mathcal{C}}_{a,k}[l; n, p] \right\|_F = \sqrt{\sum_{p=-M/2}^{M/2-1} \sum_{n=0}^{Q-1} \left| \hat{\mathcal{C}}_{a,k}[l; n, p] \right|^2} \quad (21)$$

denoting the Frobenius Norm of the LSF, as a statistical means to evaluate the stationarity of the three proposed BS conf. 1 to 3 in space. We thereby analyze if the wireless propagation channel to different RUs exhibits different statistical parameters. A value close to one indicates a similar distribution of multipath components in the delay-Doppler domain at a certain time (or equivalently in space). In contrast, a value close to zero indicates no similarity in the multipath component distribution.

The average spatial collinearity between RUs over all l is defined as

$$\bar{\gamma}_{a,a',k} = \frac{1}{\sum_{s=1}^8 |L(s)|} \sum_l \gamma_{a,a',k}[l] \quad (22)$$

and is used to assess the average value of LSF collinearity over the full UE trajectory.

IV. RESULTS OF STATISTICAL CHARACTERIZATION

In this section, we analyze the data gathered as shown in section II-A with the methods outlined in section III-A. We seek knowledge of the characteristics of each channel from user UE_1 to BS antenna a , and their relation and correlation to each other. Although ten measurement runs were obtained for each BS array configuration, the results of only one run per configuration are presented for the ease of exposition. Including more measurement runs has been analyzed and did not show significant differences in the presented results.

A. AVERAGE RECEIVED POWER

We evaluate the average received power on each individual BS antenna from transmitter UE_1 for the three considered BS array configurations along the UE trajectory. Results are normalized to the maximum average received power as defined in (19), which occurred in region R_6 with BS conf. 1. The height of the 32 bars per region indicates $10 \log_{10} \bar{\mathcal{P}}_{a,1}[s]$ and the color indicates the distance to RU 1 for each antenna in the BS array. The average normalized received power over all RUs within a region $10 \log_{10} \frac{1}{A} \sum_{a=1}^A \bar{\mathcal{P}}_{a,1}[s]$ is provided at the base of the bar plots for each region.

Figure 4 shows the average normalized received power $\bar{\mathcal{P}}_{a,1}[s]$ for regions R_1 to R_8 and BS conf. 1. Since this configuration only has a small overall aperture size of approximately 2 m (see also Fig. 3), all 32 RUs experience the same large-scale fading and $\bar{\mathcal{P}}_{a,1}[s]$ is similar within each region. In the NLOS regions R_3 to R_5 , the average received power drops 15 - 20 dB compared to the strong LOS case in region R_6 .

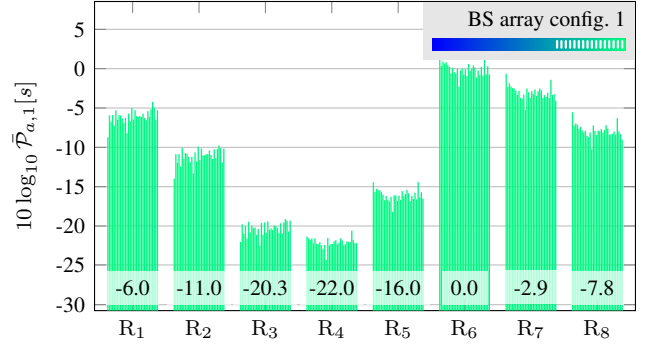


FIGURE 4: Average received power $\bar{\mathcal{P}}_{a,1}[s]$ for BS conf. 1 and regions R_1 to R_8 . Each regions contains 32 bars for all RUs. The color coding shows the respective distance to BS antenna 1 as indicated in the top right corner.

In contrast to the previous result, Fig. 5 with BS conf. 2 shows significant differences in large-scale fading along the aperture of 46.5 m. It is obvious that in this case, the common assumption of wide-sense stationarity among RUs is no longer given. The difference in average received power between the BS antenna groups (see also Fig. 3) is typically 7 - 8 dB (essentially the free space path loss between BS antenna groups), but occasionally grows as large as 20 dB like in region R_6 . In this case, RUs 1-16 have direct LOS, whereas antennas 17-32 are still blocked by the large office building to the north of the BS array. Only in region R_4 with NLOS propagation conditions and approximately the same distance from UE node to all RUs the average received power stays on a similar level over the BS aperture.

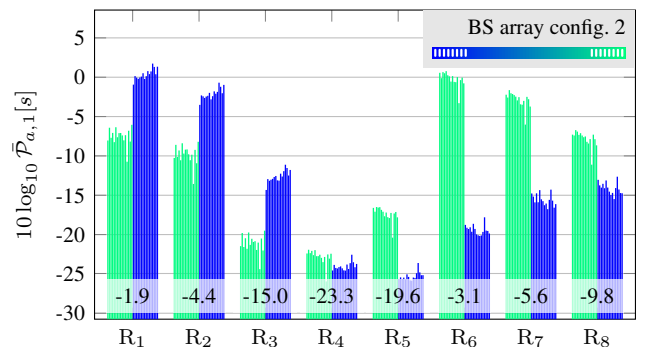


FIGURE 5: Average received power $\bar{\mathcal{P}}_{a,1}[s]$ for BS conf. 2 and regions R_1 to R_8 . Each regions contains 32 bars for all RUs. The color coding shows the respective distance to BS antenna 1 as indicated in the top right corner.

Similar to before, BS conf. 3 shows strong non-stationarity over its aperture of 46.5 m as shown in Fig. 6. Again, the differences in average received power of 7 - 8 dB in regions

R_1 to R_3 and R_5 is mostly explained with the different distance from the UE to the individual BS antenna and the corresponding path loss. Region R_6 shows the average received power with a variation of 20 dB among RUs due to a large building blocking parts of the array aperture.

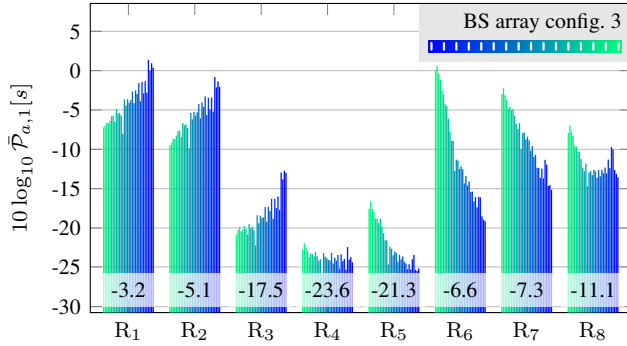


FIGURE 6: Average received power $\bar{P}_{a,1}[s]$ for BS conf. 3 and regions R_1 - R_8 . Each regions contains 32 bars for all RUs. The color coding shows the respective distance to BS antenna 1 as indicated in the top right corner.

B. DELAY- AND DOPPLER SPREADS

The large array aperture of BS conf. 2 and 3 (in relation to configuration 1) not only causes great variation in the average received power as seen in the previous section. Due to the UEs operating in the near-field, the relative distances and velocities between UEs and RUs vary greatly. To quantify this effect, we revert to the delay spread and Doppler spread as defined in (12) and (15), respectively.

A stationarity time of 256 ms for the LSF was assumed for the necessary calculations, i.e. $M = 256$. Comparative studies with a smaller stationarity time (i.e. 128 ms or 64 ms) did not show significant differences in the presented results, but offer less resolution in the Doppler domain (see (6)).

Additionally, thresholds are applied to the delay and Doppler components of the LSF to reduce influence of measurement noise and limited dynamic range on the calculation of the spreads. The noise threshold is set to 3 dB and the sensitivity threshold is set to 45 dB [17].

Delay Spread - BS Array Configuration 1

Figure 7 shows the delay spreads $\sigma_{a,1}^{(\tau)}[l]$ as defined in (12) of the $A = 32$ time-dependent channel transfer functions from UE_1 to the RUs in configuration 1. The time dependency is translated into space by plotting against the cumulative distance UE_1 traveled at each respective time instance. The color of each line indicates the distance of the respective antenna element to BS antenna 1 as indicated in the top right corner of the plot. The gray area between regions R_2 and R_6 indicates NLOS propagation conditions.

We notice that especially in the LOS regions R_1 , R_2 , and R_6 - R_8 , the delay spread is very similar among RUs, which is not surprising given the proximity of the individual array elements. In the NLOS regions R_3 to R_5 it naturally rises in general due to the lack of a strong multipath component.

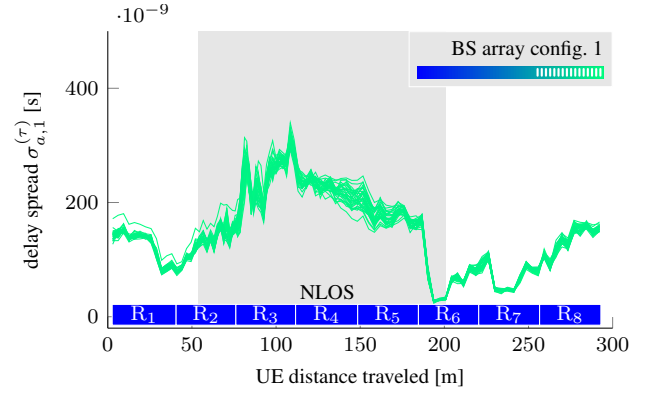


FIGURE 7: Delay spread $\sigma_{a,1}^{(\tau)}[l]$ of the $A = 32$ time-dependent channel transfer functions from UE_1 to the BS in configuration 1.

Delay Spread - BS Array Configuration 2

Figure 8 shows the delay spreads of the time-dependent channel transfer functions from UE_1 to the RUs in configuration 2. The edges of the NLOS region are indicated in light gray as only half of the RUs are blocked by the large office building. What is immediately obvious is the clustering of the delay spreads for RUs in the distributed arrays to the east and west, respectively. In regions R_1 to R_3 RUs 1-16 in the east are further from the user UE_1 than antennas 17-32, resulting in an increased delay spread. Regions R_6 to R_8 show this effect even more pronounced as the LOS to RUs 17-32 is still blocked, resulting in increased delay spreads, whereas antennas 1-16 are close to the UE trajectory and have LOS.

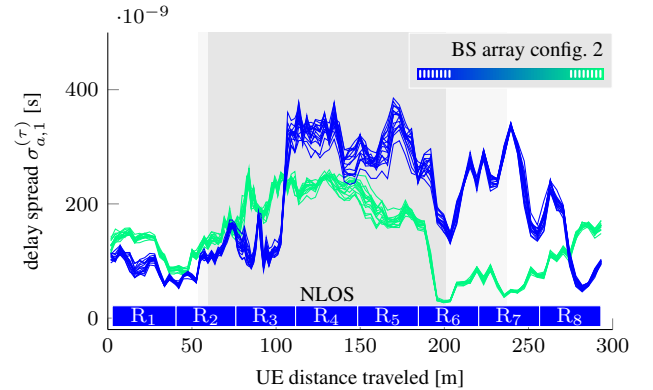


FIGURE 8: Delay spread $\sigma_{a,1}^{(\tau)}[l]$ of the $A = 32$ time-dependent channel transfer functions from UE_1 to the BS in configuration 2.

Delay Spread - BS Array Configuration 3

Figure 9 shows the delay spreads of the time-dependent channel transfer functions from UE_1 to the RUs in configuration 3. The edges of the NLOS region are fading out as the LOS to NLOS transition happens gradually over RUs. Similar to BS conf. 2, the range of occurring delay spreads for a given UE position varies widely compared to BS conf. 1. But given the uniform distribution of antenna elements, no clustering of delay spreads as in Fig. 8 is observed. Special emphasis

is put on region R_6 , where we observe a sudden drop of the delay spread of 150 ns consecutively for the RUs. This effect is caused by UE_1 emerging from the blocking building and LOS propagation conditions occurring for one BS antenna after the other.

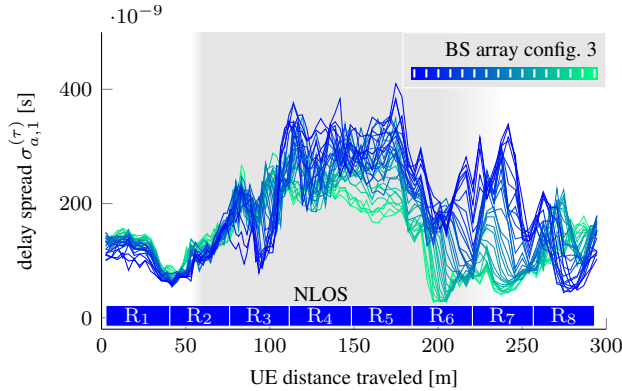


FIGURE 9: Delay spread $\sigma_{a,1}^{(\tau)}[l]$ of the $A = 32$ time-dependent channel transfer functions from UE_1 to the BS in configuration 3.

Delay Spread - Summary

Table 2 shows the quantitative analysis of the qualitative plots presented in Figs. 7 to 9. For each region R_1 to R_8 and each BS conf. 1 to 3 the maximum, minimum, mean, and standard deviation value of the delay spread over the 32 BS antenna realizations is provided.

We observe that the maximum, minimum, and mean delay spread values differ at most 20 ns for BS conf. 2 and 3, as their array aperture and position are identical (Fig. 2). The standard deviation, however, is consistently higher for the distributed massive MIMO setup in BS conf. 2. The standard deviation and therefore fluctuations in delay spread values among RUs for BS conf. 1 lies between 3 ns (LOS) and 14 ns (NLOS) and is in general significantly lower than the respective values for the BS conf. 2 and 3, given their significantly larger antenna apertures.

Doppler Spread - BS Array Configuration 1

Figure 9 shows the Doppler spread of the time-dependent channel transfer functions from UE_1 to the RUs in configuration 1. Similar to the delay spread analysis, the time dependency is translated into space by plotting against the cumulative distance UE_1 traveled at each respective time instance. The color of each line indicates the distance of the respective antenna element to BS antenna 1 as indicated in the top right corner of the plot.

As with the delay spread, also the Doppler spread variation among RUs is small at maximally 10 Hz in the LOS regions R_1 , R_2 , and R_6 to R_8 . The Doppler spread generally increases in the NLOS regions R_3 to R_5 due to the lack of a strong LOS component. The relative velocity from UE_1 to the BS was low since the UE trajectory hardly showed radial components in these regions, see Fig. 1. However, Doppler

spreads increase significantly in regions R_7 and R_8 since here the radial velocity component of the UE in relation to the BS increases.

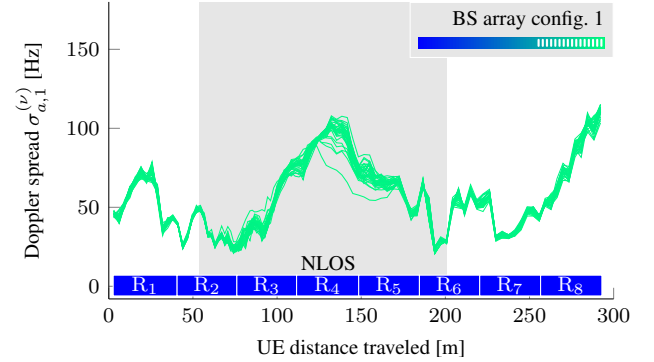


FIGURE 10: Doppler spread $\sigma_{a,1}^{(\nu)}[l]$ of the $A = 32$ time-dependent channel transfer functions from UE_1 to the BS in configuration 1.

Doppler Spread - BS Array Configuration 2

Figure 9 shows the Doppler spread of the time-dependent channel transfer functions from UE_1 to the RUs in configuration 2. Clear clustering can be observed as RUs 1-16 experience propagation and large-scale fading conditions that are different from RUs 17-32. Within each distributed group, the Doppler spread is similar among RUs. Its value is largely determined by the absence of a LOS component for the respective antenna group (regions R_3 to R_5) and the relative velocity of the UE in respect to the antenna group (regions R_6 to R_8).

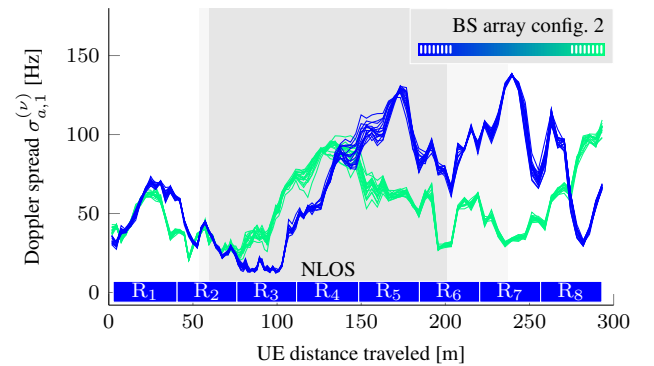


FIGURE 11: Doppler spread $\sigma_{a,1}^{(\nu)}[l]$ of the $A = 32$ time-dependent channel transfer functions from UE_1 to the BS in configuration 2.

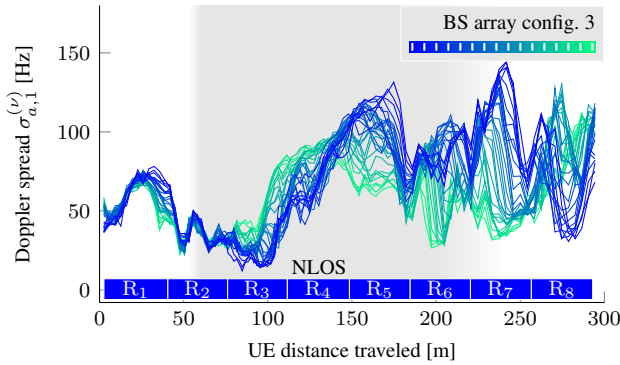
Doppler Spread - BS Array Configuration 3

Figure 9 shows the Doppler spread of the time-dependent channel transfer functions from UE_1 to the RUs in configuration 3. The minimum and maximum Doppler spread values along the trajectory of the user are, except for some outliers in region R_8 , similar. However, no clustering is observed. At each position in space along the UE trajectory, the Doppler spread values of the 32 RUs are distributed

TABLE 2: Maximum, minimum and mean value of the RMS delay spread as well as its standard deviation around the mean within regions R_1 to R_8 for BS conf. 1 to 3.

Delay spread $\sigma_{a,1}^{(\tau)}[l]$	regions							
	R_1	R_2	R_3	R_4	R_5	R_6	R_7	R_8
BS array config. 1								
Max. [ns]	181.8	213.4	344.9	317.2	251.4	179.5	133.9	193.4
Min. [ns]	72.2	72.2	120.2	164.6	93.8	22.8	37.2	78.8
Mean [ns]	119.0	133.1	230.2	229.6	178.2	72.6	73.5	138.7
Std. [ns]	5.1	9.1	14.0	11.3	11.0	5.3	3.6	6.1
BS array config. 2								
Max. [ns]	161.9	194.3	380.3	381.6	388.1	318.5	342.2	245.3
Min. [ns]	51.7	51.7	77.9	174.8	147.6	25.8	35.4	45.1
Mean [ns]	106.4	119.7	183.9	271.9	239.7	148.3	153.2	129.5
Std. [ns]	21.3	14.0	43.1	45.7	60.9	79.8	96.0	42.2
BS array config. 3								
Max. [ns]	159.1	199.9	383.6	390.8	410.8	315.7	342.1	231.0
Min. [ns]	54.0	53.4	76.8	177.3	132.4	25.8	37.5	38.0
Mean [ns]	113.4	114.9	199.3	264.2	253.9	141.0	134.3	130.8
Std. [ns]	11.7	11.7	33.7	39.2	44.8	57.2	67.5	36.2

uniformly between their minimum and maximum values. Again, sudden drops (or increases) in the Doppler spread are observed consecutively over RUs (regions R_6 , R_7) as strong signal components appear (or disappear) for the respective antenna.

**FIGURE 12:** Doppler spread $\sigma_{a,1}^{(\nu)}[l]$ of the $A = 32$ time-dependent channel transfer functions from UE_1 to the BS in configuration 3.

Doppler Spread - Summary

Table 3 shows the quantitative analysis of the qualitative plots presented in Figs. 10 to 12. For each region R_1 to R_8 and each BS conf. 1 to 3 the maximum, minimum, mean, and standard deviation value of the Doppler spread over the 32 BS antenna realizations is provided.

Many findings from analyzing the delay spreads can readily be applied to the Doppler spreads. Maximum, minimum, and mean Doppler spread values are similar (within 8 Hz in regions R_1 to R_7) for BS conf. 2 and 3, as the array aperture and position are identical. Region R_8 , however, shows an increased maximum Doppler spread that is caused

most probably by a blocking of some RUs by a large structure when the UE moves through.

The standard deviation is again and not surprisingly lowest for BS conf. 1. It is also consistently lower for the cell-free BS conf. 3 compared to the distributed configuration 2, a fact that has consequences on channel aging as detailed in Section V.

C. COLLINEARITY OF THE LSF IN SPACE

We evaluate the collinearity of the LSF in (20) to assess the stationarity of the three proposed BS conf. 1 to 3 in space, i.e. we analyze if the statistical parameters of the wireless propagation channel vary over RUs. A collinearity value close to one indicates a similar distribution of multipath components in the delay-Doppler domain, while a value close to zero indicates no similarity.

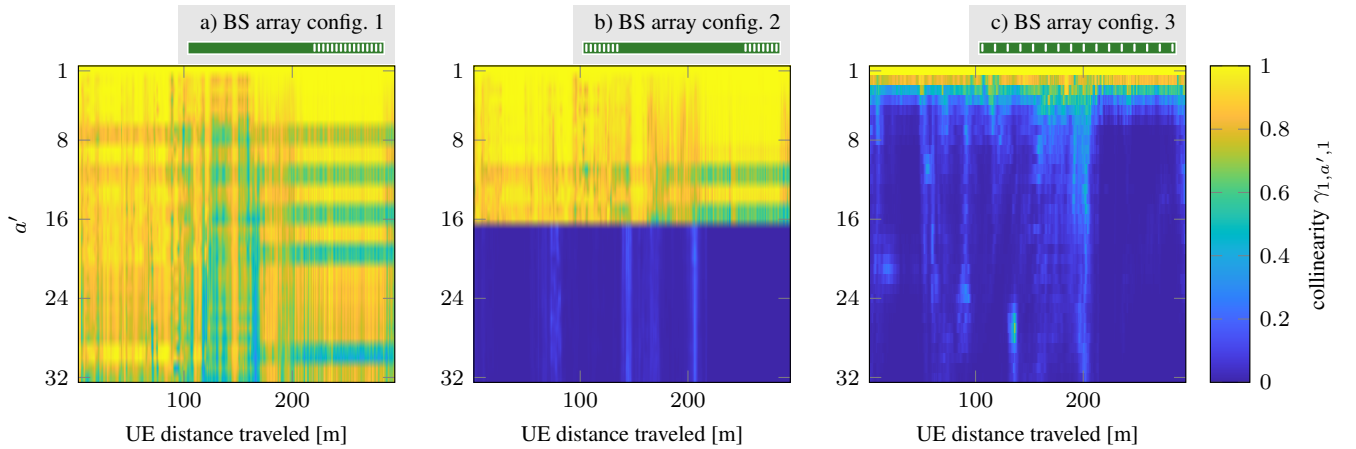
Collinearity Over Distance Traveled

Figure 13 displays the collinearity $\gamma_{a,a',1}[l]$ from BS antenna $a = 1$ to all other RUs $a' \in \{1, \dots, 32\}$ over the distance traveled by UE_1 . Figure 13 (a) for BS conf. 1 shows high collinearity values $\gamma_{a,a',1}[l]$ in general (0.8 – 1), but also exhibits regions of lower collinearity, e.g. in the NLOS regions between 100 m and 180 m traveled. Surprisingly, we do not see a monotonical decrease of collinearity with increasing RU index a' (i.e. increasing distance between RUs a' and a). Especially after 200 m distance traveled, a repetitive pattern emerges with collinearity values of 0.9 and 0.6 alternating every two antennas. The reason for this is not yet clear and subject of further investigation.

Figure 13 (b) displays the collinearity $\gamma_{a,a',1}[l]$ for BS conf. 2. The top half of the plot, representing the first BS antenna group, largely resembles the BS conf. 1 case. The bottom half of the plot, representing the RUs a' with a

TABLE 3: Maximum, minimum and mean value of the RMS Doppler spread as well as its standard deviation around the mean within regions R_1 to R_8 for BS conf. 1 to 3.

Doppler spread $\sigma_{a,1}^{(\nu)}[l]$	regions							
	R_1	R_2	R_3	R_4	R_5	R_6	R_7	R_8
BS array config. 1								
Max. [Hz]	79.6	54.0	85.5	109.8	84.6	74.1	69.2	125.4
Min. [Hz]	23.6	20.7	20.7	53.9	40.6	20.6	26.1	43.9
Mean [Hz]	53.0	32.9	44.9	87.2	62.7	47.6	42.6	84.2
Std. [Hz]	2.0	1.3	2.9	4.9	3.4	2.4	1.6	3.1
BS array config. 2								
Max. [Hz]	74.5	63.3	78.7	113.5	133.1	117.3	138.8	116.8
Min. [Hz]	27.4	18.5	11.8	41.8	45.6	25.3	27.3	28.8
Mean [Hz]	52.0	32.6	32.5	76.9	84.2	69.2	73.6	75.0
Std. [Hz]	6.6	4.0	12.2	11.5	22.5	21.0	35.7	20.9
BS array config. 3								
Max. [Hz]	78.8	68.7	85.3	116.1	132.8	120.4	145.6	131.2
Min. [Hz]	35.7	22.1	12.0	38.7	40.8	23.7	28.1	29.2
Mean [Hz]	58.9	36.2	36.0	80.6	86.7	75.5	74.8	82.6
Std. [Hz]	5.1	3.7	10.5	10.9	15.9	19.0	26.8	20.3

**FIGURE 13:** Spatial collinearity to RU $a = 1$ over distance traveled on the users trajectory for (a) BS conf. 1, (b) BS conf. 2, and (c) BS conf. 3.

distance of at least 45 m to antenna $a = 1$, does not show any significant collinearity, as expected.

Figure 13 (c) displays the collinearity $\gamma_{a,a',1}[l]$ for BS conf. 3. Already for the second BS antenna $a' = 2$, collinearity drops to 0.8 as the distance of $1.5 \text{ m} = 16\lambda$ causes significant changes in the propagation environment. This effect is also confirmed in BS conf. 1 for RUs with similar distance. For BS antenna $a' = 3$ the collinearity drops further to 0.5. We conclude that for distances larger than $3 \text{ m} = 32\lambda$, non-stationarity in space must be assumed. Additionally, a distance significantly smaller than that (i.e. $0.3 \text{ m} = 3.2\lambda$) is no guarantee for stationarity in a rich scattering environment, as seen in Fig. 13 (a).

Average Collinearity Over All Regions

We revert to the average collinearity over all regions R_1 to R_8 as defined in (22) to analyze collinearity between all BS

antenna pairs (a, a') . This allows us to assess stationarity of antenna groups within the BS array in space.

Figure 13 (a) displays the average collinearity $\bar{\gamma}_{a,a',1}[l]$ for BS conf. 1. Overall, collinearity of the involved LSFs is high at values between 0.9 and 1. However, RUs with indices $a \in \{7, 8, 11, 12, 15, 16, 19, 20, 29, 30\}$ apparently exhibit differing propagation characteristics as the complimentary BS antenna set and therefore low collinearity at 0.6 – 0.7, thus yielding the observed checkerboard pattern.

Figure 13 (b) displays the average collinearity $\bar{\gamma}_{a,a',1}[l]$ for BS conf. 2. The observations from above are immediately applicable to each 16×16 block on the main diagonal, i.e. the distributed BS antenna array groups exhibit high collinearity within themselves, but not among them. Collinearity between any RU in the east ($a \in \{1, \dots, 16\}$) and in the west ($a \in \{17, \dots, 32\}$) is negligible.

Figure 13 (c) displays the average collinearity $\bar{\gamma}_{a,a',1}[l]$ for

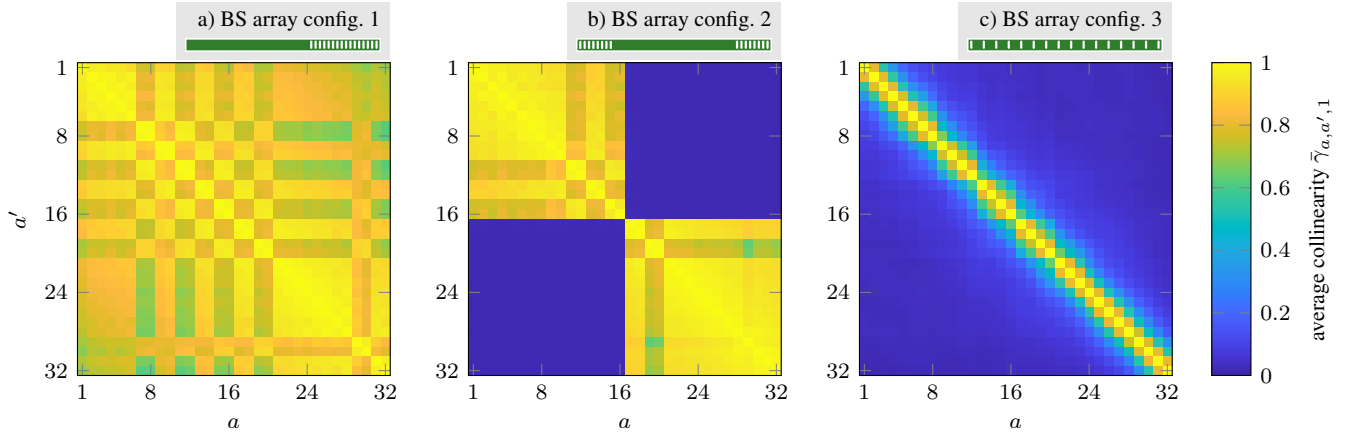


FIGURE 14: Average spatial collinearity over all regions for all RU combinations (a, a') and for (a) BS conf. 1, (b) BS conf. 2, and (c) BS conf. 3.

BS conf. 3. In this configuration, the distance between consecutive RUs is 1.5 m and therefore the collinearity decreases rapidly, i.e. to 0.8 for $|a' - a| = 1$ and to 0.5 for $|a' - a| = 2$. We conclude that there is no antenna pair (a, a') for which stationarity holds if their distance is larger than $3 \text{ m} = 32\lambda$.

D. KEY FINDINGS

Summarizing this result section, we note the following.

- Large-scale fading and shadowing cause path-loss differences of up to 20 dB over horizontal linear BS array apertures that are 46.5 m in size for the scenario under investigation.
- The delay and Doppler spread vary greatly, up to 300 ns and 100 Hz respectively, over the aperture size for BS conf. 2 and 3.
- The standard deviation of the delay spread and the Doppler spread over RU realizations is larger for BS conf. 2 than for configuration 3.
- Stationarity in space among RUs is likely for aperture sizes below $2 \text{ m} = 21\lambda$, but not guaranteed.
- Non-stationarity in space among RUs can be assumed for BS antenna distances greater than $3 \text{ m} = 32\lambda$.

V. MASSIVE MIMO PROCESSING AND RESULTS

The unmatched spectral efficiency of massive MIMO systems [20] arises due to K users being served by a large number of RUs $A \gg K > 1$ in favorable propagation conditions within a rich scattering environment.

A common step to simplify analysis in literature is to assume the matrix describing the wireless channel to be composed of independent and identically distributed (i.i.d.) channel realizations for the RUs a . With the growing array aperture size of distributed massive MIMO and cell-free systems, and the resulting variation in large-scale fading, shadowing, and relative velocities over RUs, as shown in the previous section, this assumption no longer holds. It is therefore not sufficiently known in the community if the linear processing algorithms commonly utilized in massive

MIMO maintain their close-to-optimal performance in cell-free systems.

In the following, we utilize the wireless channel measurements described in Section II and Section III to derive a massive MIMO signal model with channel matrix realizations deduced from real-world propagation scenarios. These channel matrices obtain their characteristics solely from the geometric relation between users and BS and all the scattering and blocking objects in their surroundings as shown in Fig. 1. No statistical or other modeling assumptions for the channel matrix are made.

A. MASSIVE MIMO SIGNAL MODEL

We consider an uplink massive MIMO system where $K = 2$ users UE_k are transmitting to a BS deploying A antennas. The channel vector for user k at symbol index m is constructed by assembling the coherently measured and sampled channel transfer function $\hat{H}_{a,k}[m]$ from (5) into vector form,

$$\mathbf{h}_{k,m} = [\hat{H}_{0,k}[m], \hat{H}_{1,k}[m], \dots, \hat{H}_{A-1,k}[m]]^T \in \mathbb{C}^{A \times 1}. \quad (23)$$

The channel vector collects the channel coefficients from user k to all A RUs. The frequency index q , which is interpreted as a subcarrier index in this context, is dropped as all following analysis only considers one subcarrier at a time.

The channel vectors of all users are grouped into the channel matrix (refer to [21] for more details)

$$\mathbf{H}_m = [\mathbf{h}_{0,m}, \mathbf{h}_{1,m}, \dots, \mathbf{h}_{K-1,m}], \quad (24)$$

where in our case, $K = 2$ as two distinct transmitters were utilized in the channel sounding campaign.

By applying a beamforming matrix $\mathbf{W}_m = [\mathbf{w}_{0,m}, \mathbf{w}_{1,m}, \dots, \mathbf{w}_{K-1,m}] \in \mathbb{C}^{A \times K}$ in the uplink, the vector collecting the received uplink symbols from all K users is

$$\tilde{\mathbf{y}}_m = \mathbf{W}_m^H \mathbf{H}_m \mathbf{x}_m + \frac{1}{\sqrt{P}} \tilde{\mathbf{z}}_m \quad (25)$$

with P the average transmit power of each user, \mathbf{x}_m the vector collecting the transmit symbols of each user, and

$\frac{1}{\sqrt{P}}\tilde{\mathbf{z}}_m = \frac{1}{\sqrt{P}}\mathbf{W}_m^H \mathbf{z}_m \sim \mathcal{CN}\left(0, \frac{\sigma^2}{P}\mathbf{I}_K\right)$ filtered complex Gaussian noise.

The received symbol from user k at the BS then reads as

$$\tilde{y}_{k,m} = \mathbf{w}_{k,m}^H \mathbf{h}_{k,m} x_{k,m} + \frac{1}{\sqrt{P}}\tilde{z}_{k,m} + \sum_{k' \neq k} \mathbf{w}_{k,m}^H \mathbf{h}_{k',m} x_{k',m} \quad (26)$$

where the first term is the desired signal, the second term is filtered and scaled Gaussian noise $\frac{1}{\sqrt{P}}\tilde{z}_{k,m} \sim \mathcal{CN}\left(0, \frac{\sigma^2}{P}\right)$, and the third term is interference from other users $k' \neq k$.

Note that the measurement framework shown in section II-A in itself does not introduce any inter-user interference as the users transmit their respective sounding sequence separated in time. However, interpreting the measured channel transfer function as entries in the channel matrix (24) provides a signal model that assumes simultaneous transmission of all users, thus yielding the interference term in (26).

The performance of a massive MIMO systems in terms of SINR (or equivalently spectral efficiency) is largely determined by the properties of the current channel matrix realization \mathbf{H}_m and its statistics. We therefore establish in the following the methods to assess the characteristics of the channel matrix and, ultimately, the quality of a wireless communication system based on it.

SINR and Channel Aging

Rate and reliability for user k are mainly determined by the instantaneous SINR

$$\text{SINR}_{k,m} = \frac{|\mathbf{w}_{k,m}^H \mathbf{h}_{k,m}|^2}{\frac{\sigma^2}{P} + \sum_{k' \neq k} |\mathbf{w}_{k,m}^H \mathbf{h}_{k',m}|^2} \quad (27)$$

defined as the ratio of the signal component to the interference and noise component in (26). We consider in what follows the beam-forming vectors $\mathbf{w}_{k,m}$ to being calculated via the zero-forcing (ZF) approach by solving

$$\mathbf{W}_m = [\mathbf{w}_{0,m}, \mathbf{w}_{1,m}, \dots, \mathbf{w}_{K-1,m}] \quad (28)$$

$$= \tilde{\mathbf{H}}_{m,\Delta t} \left(\tilde{\mathbf{H}}_{m,\Delta t}^H \tilde{\mathbf{H}}_{m,\Delta t} \right)^{-1}. \quad (29)$$

To quantify the effect of channel aging, we deliberately introduce outdated channel matrices to calculate the beam-forming matrices in (29). The outdated channel matrix $\tilde{\mathbf{H}}_{m,\Delta t}$ is defined similar to (24) as the outdated channel vectors $\tilde{\mathbf{h}}_{k,m,\Delta t}$ grouped into a matrix, i.e.

$$\tilde{\mathbf{H}}_{m,\Delta t} = [\tilde{\mathbf{h}}_{0,m,\Delta t}, \tilde{\mathbf{h}}_{1,m,\Delta t}, \dots, \tilde{\mathbf{h}}_{K-1,m,\Delta t}], \quad (30)$$

$$\tilde{\mathbf{h}}_{k,m,\Delta t} = [\hat{H}_{0,k}(mT_R + \Delta t), \hat{H}_{1,k}(mT_R + \Delta t), \dots, \hat{H}_{A-1,k}(mT_R + \Delta t)]^T. \quad (31)$$

The channel transfer functions $\hat{H}_{a,k}(mT_R + \Delta t)$ that were not measured directly are obtained by interpolating the preceding and subsequent measured channel transfer functions $\hat{H}_{a,k}[m'] = \hat{H}_{a,k}(m'T_R)$, $m' \in \{m-2, m-1, m, m+1\}$

using a cubic spline interpolation [22], [23]. This approach works sufficiently well since the repetition rate of the channel sounding measurements $T_R = 1$ ms is high enough to periodically capture channel transfer function realizations while the users move maximally $1.7 \text{ cm} = 0.18\lambda$ at their maximum velocity of 60 km/h [24].

The beam-forming matrix \mathbf{W}_m determines the ability of a massive MIMO system to maximize the signal component and minimize interference from other users. Acquisition of timely CSI (i.e. with small delay Δt) $\tilde{\mathbf{H}}_{m,\Delta t} \approx \mathbf{H}_m$ that is necessary to calculate the beam-forming matrix is, however, non-trivial if high mobility is involved. By the time the beam-forming matrix is applied, it might already be out-dated (i.e. $\tilde{\mathbf{H}}_{m,\Delta t} \not\approx \mathbf{H}_m$) and the instantaneous SINR in (27) decreases. This effect is called *channel aging* and prevents massive MIMO systems to operate in high mobility scenarios without special measures such as channel prediction [4].

Minimum mean square error (MMSE) beam-forming is not considered because its benefits over ZF are negligible in the high SNR regime investigated in this work (i.e. CSI is acquired during a channel sounding campaign where the UE transmit power is 38 dBm and the measurement SNR is greater than 25 dB at all times).

Channel Hardening

The large number of RUs $A \gg K \gg 1$ leads to linear beam-forming (e.g. ZF as outlined above) being close to optimal. Additionally, the law of large numbers guarantees that random fluctuations of the signal component $|\mathbf{w}_{k,m}^H \mathbf{h}_{k,m}|^2$ become less probable and the effective channel $\mathbf{w}_{k,m}^H \mathbf{h}_{k,m}$ becomes quasi-deterministic – a process called *channel hardening* [25].

As a measure for channel hardening, we revert to the signal component's ratio of the standard deviation estimation to its estimated mean over M consecutive time indices

$$\gamma_{k,l} = \frac{\sqrt{\frac{1}{M-1} \sum_{m=-M/2+1}^{M/2-1+1} \left(|\mathbf{w}_{k,m}^H \mathbf{h}_{k,m}|^2 - \mu_{k,l} \right)^2}}{\mu_{k,l}} \quad (32)$$

$$\mu_{k,l} = \frac{1}{M} \sum_{m=-M/2+1}^{M/2-1+1} |\mathbf{w}_{k,m}^H \mathbf{h}_{k,m}|^2 \quad (33)$$

which tends to zero as the channel becomes more and more deterministic.

B. MASSIVE MIMO RESULTS

This section presents the results for the instantaneous SINR, channel aging and channel hardening derived from the measurement results obtained as described in section II and the signal model introduced in section V-A. The measured channel transfer function realizations are directly interpreted as channel vector realizations as defined in (23).

SINR and Channel Aging Results

The instantaneous SINR (27) determines achievable rates for the respective user k at a given time instant m . The signal component in the numerator and the interference component in the denominator heavily depend on the beam-forming applied at the BS, which in turn relies on timely CSI. We analyze the influence of aged CSI on the instantaneous SINR by calculating the beam-forming matrix (29) with outdated channel matrices $\tilde{\mathbf{H}}_{m,\Delta t}$ that are delayed by $\Delta t \in \{10 \mu\text{s}, 100 \mu\text{s}, 500 \mu\text{s}\}$.

Figure 15 plots the empirical CDF of the SINR (27) for outdated channel matrices (vertically aligned) and different regions (horizontally aligned). To calculate the empirical CDF, all channel matrices obtained in a given region (in which the UEs move along their trajectory) are used to calculate (29) and in turn the SINR. Each subplot in Fig. 15 shows the three BS conf. 1 to 3 under consideration in this paper. Regions R_1 and R_6 exhibit LOS propagation characteristics while region R_4 is purely NLOS, see Fig. 1.

In region R_1 and with small channel aging of $\Delta t = 10 \mu\text{s}$, BS conf. 3 shows the highest SINR values on average, and BS conf. 2 performs slightly worse. BS conf. 1, however, has a significant drawback since the average distance between RUs and UEs is highest in this configuration (the larger aperture of configuration 2 and 3 lead to RUs being closer to the UE trajectory). The SINR is on average 3 dB lower in this configuration.

When the delay between CSI acquisition and beam-forming increases to $\Delta t = 100 \mu\text{s}$, the BS array configuration most affected is BS conf. 2 which now only shows slightly higher average SINR values than configuration 1. BS configuration 1 and 3 largely maintain the distribution of the empirical CDF. For all three configurations, the effect of channel aging is already noticeable.

For a delay between CSI acquisition and beam-forming of $\Delta t = 500 \mu\text{s}$, as depicted in Fig. 15 at the bottom left, the SINR drops significantly for all BS conf. 1 to 3. Specifically, the median SINR value over the region R_1 drops by 7 dB in configuration 1, 11 dB in configuration 2, and 8 dB in configuration 3, compared to hardly any channel aging (at a CSI delay of $10 \mu\text{s}$).

The comparatively small effects of channel aging in region R_1 on BS conf. 1 is explained by the small relative velocity of the UEs in relation to the BS. Both configuration 2 and 3 feature RUs which are closer to the UE trajectory, but therefore also exhibit larger Doppler spreads, see also Fig. 11.

In region R_4 with NLOS propagation conditions, depicted in the center column of Fig. 15, channel aging has only very limited effect on the empirical CDF of the SINR. The median drops by at most 1.5 dB for all BS array configurations, comparing $\tilde{\mathbf{H}}_{m,\Delta t}$ aged $10 \mu\text{s}$ and $500 \mu\text{s}$, respectively. Again, BS conf. 3 shows the least sensitivity to channel aging.

In region R_6 , the right-most column in Fig. 15, BS conf. 1 shows the clear advantage of having all RUs close to the current position of the UEs and in direct LOS, whereas for both configuration 2 and 3 a considerable amount of antennas

are still blocked by a large office building. Therefore, both large aperture configurations 2 and 3 give a similar SINR distribution that is in general shifted to lower values when compared to BS conf. 1. However, also in region R_6 BS conf. 3 is less influenced by channel aging of $\Delta t = 500 \mu\text{s}$, with its median SINR value dropping only 6 dB as compared to 10 dB and 8 dB of configuration 1 and 2, respectively.

Channel Hardening Results

An evaluation of the channel hardening coefficient (32) distribution in regions R_1 (LOS), R_4 (NLOS), and R_6 (LOS) is shown in Fig. 16. It is immediately evident that channel hardening, i.e. the random fluctuations of the signal component $|\mathbf{w}_{k,m}^H \mathbf{h}_{k,m}|^2$ in (27), is lowest for the BS conf. 3 in all regions. This leads to the conclusion that if deterministic signal levels are desired, cell-free configurations improve on the channel hardening capabilities of conventional massive MIMO systems.

C. KEY FINDINGS

Summarizing the massive MIMO processing result section, we note the following.

- Cell-free systems are less susceptible to channel aging than distributed or conventional massive MIMO systems as presented in Fig. 15. The exact reason behind this phenomenon is still under investigation, but we suspect that the wide range of relative velocities of the UE in relation to the RUs (see the Doppler spreads in Fig. 9) mitigates channel aging to some extent.
- Cell-free systems offer better channel hardening capabilities than distributed or conventional massive MIMO systems as presented in Fig. 16 due to the great variation in multipath distribution over RUs (see also Fig. 14).

VI. CONCLUSION

In this paper we investigated radio wave propagation conditions of cell-free widely distributed massive MIMO systems to confirm the merits promised by signal processing theory. In such systems radio units are spread out over a large geographical region and the radio signal of a UE is coherently detected by a subset of RUs in the vicinity of the UE and processed jointly at the nearest BPU. Cell-free systems promise two orders of magnitude less transmit power, spatial focusing at the UE position for high reliability, and consistent throughput over the coverage area. However, these properties have been investigated only from a theoretical point of view so far.

We presented a SDR based measurement system and an analysis of empirical radio wave propagation measurements in the form of time-variant channel transfer functions for a linear widely distributed antenna array with 32 single antenna RUs spread out over a range of 46.5 m. Three different co-located and widely distributed RU configurations and their properties in an urban environment have been analyzed in terms of time-variant delay-spread, Doppler spread, path loss and the correlation of the local scattering function over space.

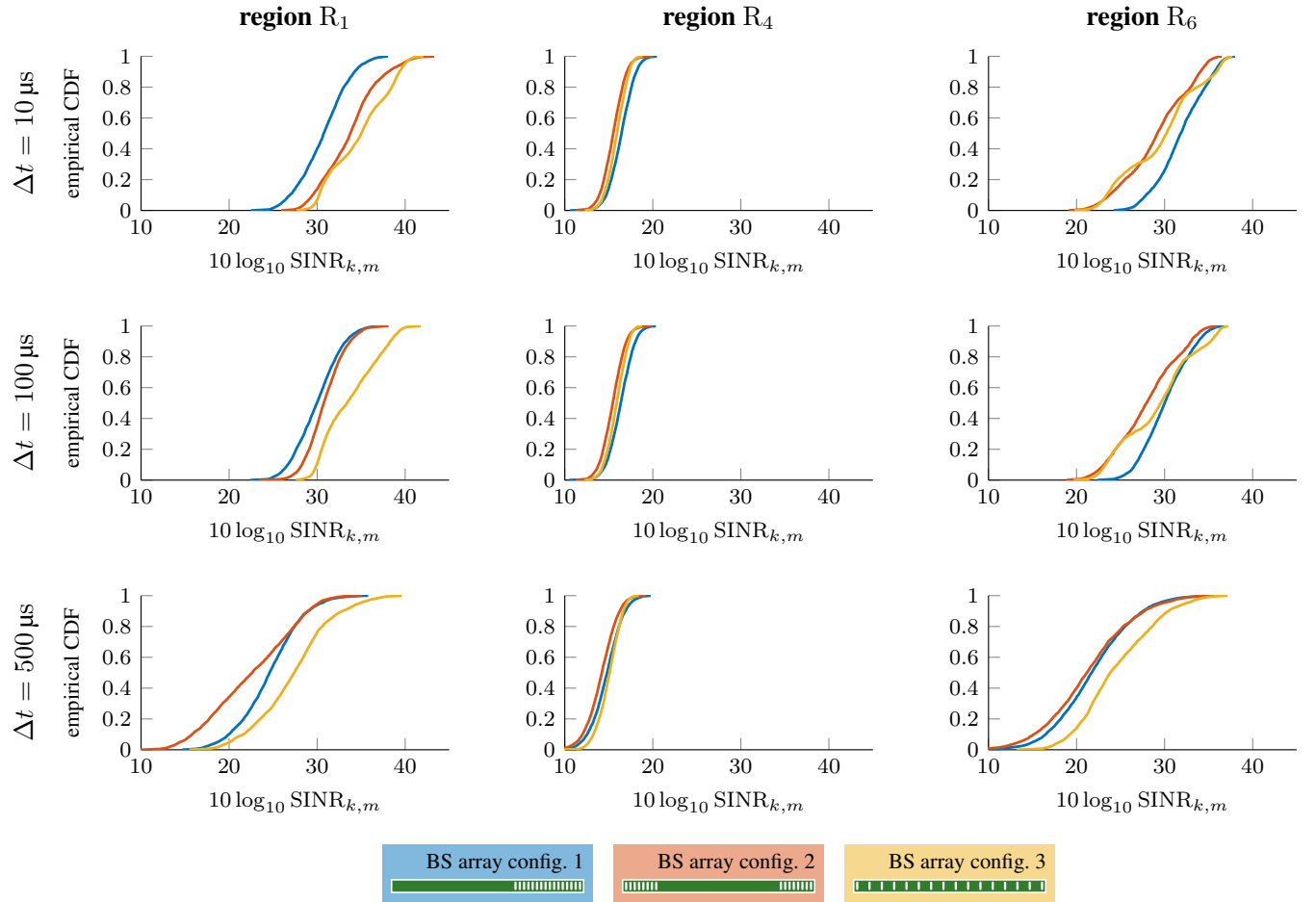


FIGURE 15: Empirical cumulative distribution function (CDF) of the SINR for regions R_1 (left), R_4 (middle) and R_6 (right), BS conf. 1 to 3, and channel matrices $\mathbf{H}_{m,\Delta t}$ aged $\Delta t = 10 \mu\text{s}$ (top), $\Delta t = 100 \mu\text{s}$ (middle), and $\Delta t = 500 \mu\text{s}$ (bottom).

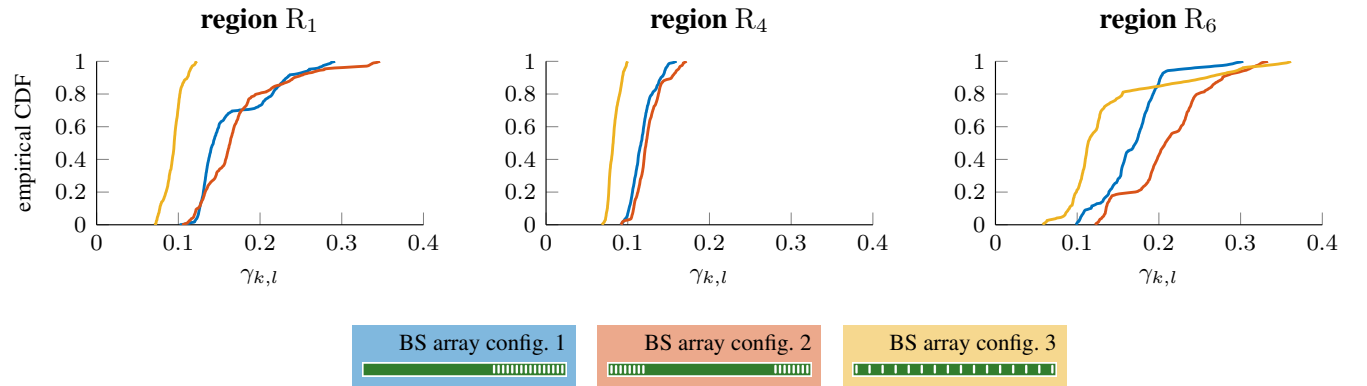


FIGURE 16: Empirical CDF of the channel hardening coefficient $\gamma_{k,l}$ for regions R_1 , R_4 and R_6 , and BS conf. 1 to 3.

The path loss from the UE over all RUs shows a maximal variation of 5 dB for a closely spaced linear array (0.64λ spacing, BS conf. 1) and a variation of 20 dB for the widely distributed massive MIMO array (16λ spacing, BS conf. 3). The strongest difference can be observed in the transition phase from LOS to NLOS.

The variance of the RMS delay and RMS Doppler-spread

is smallest for the co-located BS conf. 1 and increases with the aperture of the antenna arrays. Hence, the widely distributed BS conf. 2 and 3 exhibit an increased range of RMS delay spread (300 ns) and Doppler spread (100 Hz) over all 32 RUs. Also here the strongest variation is caused by the transition from NLOS to LOS.

The stationarity in space among RUs was validated to

be likely for an aperture size smaller than $2m = 21\lambda$, although it is not guaranteed to hold. For apertures larger than $3m = 32\lambda$, non-stationary properties have been confirmed by means of the collinearity of the LSF in space.

For the development of 6G cell-free massive MIMO transceiver algorithms, we analyzed properties such as channel hardening, channel aging and its influence on the SINR. Channel aging shows the strongest impact in LOS regions for all three measured configurations. BS conf. 3 exhibits the best SINR for long aging intervals in both LOS and NLOS conditions, even with less received power. For channel hardening, the widely-distributed BS conf. 3 provides the strongest effect compared to BS conf. 1 and 2 for LOS as well as NLOS scenarios.

Our empirical evidence, summarized above, supports the promising claims for widely distributed user-centric cell-free systems as a revolutionary new 6G architecture.

REFERENCES

- [1] Ö. T. Demir, E. Björnson, L. Sanguinetti et al., "Foundations of user-centric cell-free massive MIMO," *Foundations and Trends in Signal Processing*, vol. 14, no. 3-4, pp. 162–472, 2021.
- [2] J. Zhang, S. Chen, Y. Lin, J. Zheng, B. Ai, and L. Hanzo, "Cell-free massive MIMO: A new next-generation paradigm," *IEEE Access*, vol. 7, pp. 99 878–99 888, 2019.
- [3] D. Löschenbrand, M. Hofer, L. Bernadó, G. Humer, B. Schrenk, S. Zelenbaba, and T. Zemen, "Distributed massive MIMO channel measurements in urban vehicular scenario," in *13th European Conference on Antennas and Propagation (EuCAP)*, 2019, pp. 1–5.
- [4] D. Löschenbrand, M. Hofer, and T. Zemen, "Orthogonal precoding with channel prediction for high mobility massive MIMO," in *IEEE International Symposium on Personal, Indoor and Mobile Radio Communications (PIMRC)*, 2020.
- [5] H. I. Obakhena, A. L. Imoize, F. I. Anyasi, and K. Kavitha, "Application of cell-free massive MIMO in 5G and beyond 5G wireless networks: A survey," *Journal of Engineering and Applied Science*, vol. 68, no. 1, pp. 1–41, 2021.
- [6] G. Interdonato, E. Björnson, H. Quoc Ngo, P. Frenger, and E. G. Larsson, "Ubiquitous cell-free massive MIMO communications," *EURASIP Journal on Wireless Communications and Networking*, vol. 2019, no. 1, pp. 1–13, 2019.
- [7] S. Payami and F. Tufvesson, "Channel measurements and analysis for very large array systems at 2.6 GHz," in *2012 6th European Conference on Antennas and Propagation (EUCAP)*, 2012, pp. 433–437.
- [8] À. O. Martínez, E. D. Carvalho, and J. Ø. Nielsen, "Towards very large aperture massive MIMO : a measurement based study," in *IEEE Globecom Workshops*, 2014, pp. 281–286.
- [9] T. Choi, M. Ito, I. Kanno, T. Oseki, K. Yamazaki, and A. F. Molisch, "Uplink energy efficiency of cell-free massive MIMO with transmit power control in measured propagation channels," in *2021 IEEE Workshop on Signal Processing Systems (SiPS)*, 2021, pp. 164–169.
- [10] T. Choi, J. Gomez-Ponce, C. Bullard, I. Kanno, M. Ito, T. Ohseki, K. Yamazaki, and A. F. Molisch, "Using a drone sounder to measure channels for cell-free massive MIMO systems," 2021.
- [11] A. F. Molisch, F. Tufvesson, J. Karedal, and C. F. Mecklenbrauker, "A survey on vehicle-to-vehicle propagation channels," *IEEE Wireless Communications*, vol. 16, no. 6, pp. 12–22, 2009.
- [12] D. Löschenbrand, M. Hofer, B. Rainer, and T. Zemen, "Empirical and simulated performance evaluation of distributed massive MIMO," in *Asilomar Conference on Signals, Systems, and Computers (ASILOMAR)*, 2019, pp. 1–5.
- [13] A. F. Molisch, *Wireless Communications*, 2nd ed. John Wiley & Sons, 2011.
- [14] M. Friese, "Multitone signals with low crest factor," *IEEE Transactions on Communications*, vol. 45, no. 10, pp. 1338–1344, 1997.
- [15] G. Matz, "On non-WSSUS wireless fading channels," *IEEE Transactions on Wireless Communications*, vol. 4, no. 5, pp. 2465–2478, 2005.
- [16] A. Paier, T. Zemen, L. Bernadó, G. Matz, J. Karedal, N. Czink, C. Dumard, F. Tufvesson, A. F. Molisch, and C. F. Mecklenbrauker, "Non-WSSUS vehicular channel characterization in highway and urban scenarios at 5.2 GHz using the local scattering function," in *2008 International ITG Workshop on Smart Antennas*, 2008, pp. 9–15.
- [17] L. Bernadó, T. Zemen, F. Tufvesson, A. F. Molisch, and C. F. Mecklenbrauker, "Delay and Doppler spreads of nonstationary vehicular channels for safety-relevant scenarios," *IEEE Trans. Veh. Technol.*, vol. 63, no. 1, pp. 82–93, Jan. 2014.
- [18] D. Slepian, "Prolate spheroidal wave functions, Fourier analysis, and uncertainty-V: The discrete case," *Bell Syst. Technol. J.*, vol. 57, no. 5, pp. 1371–1430, May 1978.
- [19] E. Zöchmann, M. Hofer, M. Lerch, S. Pratschner, L. Bernadó, J. Blumenstein, S. Caban, S. Sangodoyin, H. Groll, T. Zemen, A. Prokeš, M. Rupp, A. F. Molisch, and C. F. Mecklenbrauker, "Position-specific statistics of 60 GHz vehicular channels during overtaking," *IEEE Access*, vol. 7, pp. 14 216–14 232, 2019.
- [20] T. L. Marzetta, "Noncooperative cellular wireless with unlimited numbers of base station antennas," *IEEE Transactions on Wireless Communications*, vol. 9, no. 11, pp. 3590–3600, 2010.
- [21] K. T. Truong and R. W. Heath, "Effects of channel aging in massive MIMO systems," *Journal of Communications and Networks*, vol. 15, no. 4, pp. 338–351, 2013.
- [22] S. McKinley and M. Levine, "Cubic spline interpolation," *College of the Redwoods*, vol. 45, no. 1, pp. 1049–1060, 1998.
- [23] C. De Boor and C. De Boor, *A Practical Guide To Splines*. Springer-Verlag New York, 1978, vol. 27.
- [24] S. Coleri, M. Ergen, A. Puri, and A. Bahai, "Channel estimation techniques based on pilot arrangement in OFDM systems," *IEEE Transactions on Broadcasting*, vol. 48, no. 3, pp. 223–229, 2002.
- [25] T. Zemen, D. Löschenbrand, M. Hofer, C. Pacher, and B. Rainer, "Orthogonally precoded massive MIMO for high mobility scenarios," *IEEE Access*, vol. 7, pp. 132 979–132 990, 2019.



DAVID LÖSCHENBRAND received the Dipl.-Ing. degree (with distinction) in Telecommunications in 2016 from Vienna University of Technology. From 2012 to 2015, he worked for the Institute of Telecommunications, implementing software for antenna characterization purposes. Since 2016, he is a Ph.D. candidate with the AIT Austrian Institute of Technology in Vienna, Austria. His research focuses on massive MIMO in time-varying propagation channels, channel aging, antenna design, reliable low-latency wireless communications for highly autonomous vehicles, vehicular channel measurements and channel modeling. He gained experience in research work and project management during several finished and ongoing applied research projects on a national and international scale. He implemented a software defined radio based cell-free massive MIMO testbed for coherent measurements and signal processing experimentation.



MARKUS HOFER received the Dipl.-Ing. degree (with distinction) in telecommunications from the Vienna University of Technology, Vienna, Austria, in 2013 and the doctoral degree in 2019. From 2013 to 2015 he was with the FTW Telecommunications Research Center Vienna working as a Researcher in the Signal and Information Processing department. He has been with the AIT Austrian Institute of Technology, Vienna since 2015 and is working as a Scientist in the research group for

ultrareliable wireless machine-to-machine communications. His research interests include ultra-reliable low latency wireless communications, reflective intelligent surfaces, mmWave communications, cell-free massive MIMO, time-variant channel measurements, modeling and realtime emulation; time-variant channel estimation, 5G massive MIMO systems; software-defined radio rapid prototyping, cooperative communication systems, and interference management.

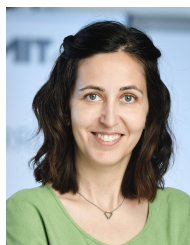


THOMAS ZEMEN (S'03-M'05-SM'10) received the Dipl.-Ing. degree in electrical engineering in 1998, the doctoral degree in 2004 and the Venia Docendi (Habilitation) in 2013, all from Vienna University of Technology. He is Principal Scientist at the AIT Austrian Institute of Technology, Vienna, Austria, leading the reliable wireless communications group. Previously he worked at the Telecommunication Research Center Vienna (FTW) and Siemens Austria.

Mr. Zemen is the author or coauthor of four books chapters, 37 journal papers and more than 113 conference communications. His research interests focus on the interaction of the physical radio communication channel with other parts of a communication system for time-sensitive 5G and 6G applications.

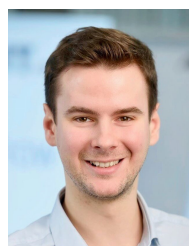
Dr. Zemen is docent at the Vienna University of Technology and served as Editor for the IEEE Transactions on Wireless Communications from 2011 - 2017

...



LAURA BERNADÓ obtained her PhD in telecommunications engineering from the Vienna University of Technology (VUT) in 2012 and the M.Sc. degree in telecommunications engineering from the Technical University of Catalonia (UPC) in 2007, with the Master Thesis written at the Royal Institute of Technology (KTH), in Stockholm. Mrs. Bernadó has worked as a researcher in the signal and information processing department at the Telecommunications Research Center in

Vienna, Austria, for 6 years, and as an antenna engineer at Fractus SA, Spain, for 3 years. Currently she works a scientist in the reliable wireless communications research group at the department for digital safety and security at AIT Austrian Institute of Technology. Her research interests are modeling of fast time-varying non-stationary fading processes, channel emulation and transceiver design for ultra-reliable wireless communication systems.



STEFAN ZELENBABA graduated from the Faculty of Electrical Engineering of University of Belgrade, Telecommunications Engineering in 2015, and received his Master's degree in collaboration with Nokia Bell Labs in 2017. Since 2017 he is a Ph.D. candidate with the Austrian Institute of Technology in the reliable wireless communications research group of Thomas Zemen. His research is focused on measurements and characterization of non-stationary time-variant wireless

channels as well as geometry-based wireless channel models and their validation.